

1 **New Insights into the Dynamics that Control the Activity of Ceria-Zirconia Solid**
2 **Solutions in Thermochemical Water Splitting Cycles**

3
4 A. Pappacena,[†] M. Rancan,^{‡,□} L. Armelao,^{‡,□} J. Llorca,[§] W. Ge,^{||} B. Ye,^{||} A. Lucotti,[‡]
5 A. Trovarelli,[†] M. Boaro^{*,†}

6 [†] *Dipartimento Politecnico di Ingegneria e Architettura, Università di Udine, Via del Cotonificio*
7 *108, 33100 Udine, Italy*

8 [‡] *Istituto di Chimica della Materia Condensata e di Tecnologie per l'Energia (ICMATE) –*
9 *Consiglio Nazionale delle Ricerche (CNR), Via Marzolo 1, 35131 Padova (Italy).*

10 [□] *Dipartimento di Scienze Chimiche, Università di Padova, Via Marzolo 1, 35131 Padova (Italy).*

11 [§] *Institut de Tècniques Energètiques and Barcelona Research Center in Multiscale Science and*
12 *Engineering, Universitat Politècnica de Catalunya, EEBE, Eduard Maristany 10-14, 08019*
13 *Barcelona, Spain*

14 ^{||} *State Key Laboratory of Particle Detection and Electronics, University of Science and Technology*
15 *of China, Hefei, 230026, P. R. China*

16 [‡] *Dipartimento di Chimica, Materiali ed Ingegneria Chimica "G. Natta", Politecnico di Milano,*
17 *Piazza Leonardo da Vinci, 32 – 20133 Milano, Italy.*

18

19

20

21

22

23

24

25

26

27

28

29

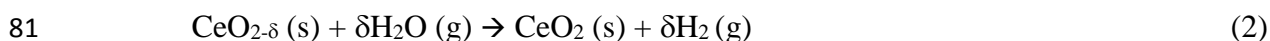
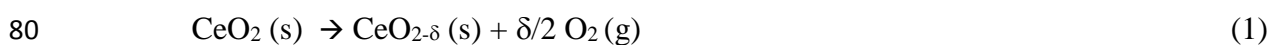
30

ABSTRACT

The reactivity of a ceria-rich $\text{Ce}_{0.85}\text{Zr}_{0.15}\text{O}_2$ solid solution towards the thermochemical water splitting process (TWS) was studied over repeated $\text{H}_2/\text{H}_2\text{O}$ redox cycles. The structural and surface modifications after treatment at high temperature under air or N_2 atmospheres were characterized by High-Resolution Transmission Electron Microscopy (HRTEM), X-ray diffraction (XRD), Raman spectroscopy, X-ray Photoemission Spectroscopy (XPS) and Positron Annihilation Lifetime Spectroscopy (PALS). Samples treated under nitrogen resulted more active due to phase segregation with formation of a zirconyl oxynitride phase in catalytic amount. Insertion of N^{3-} into the structure contributes to increase the numbers of oxygen vacancies that preferably arrange in large clusters, and to stabilize Ce^{3+} centers on the surface. In comparison, treatment under air resulted in a different arrangement of defects with less Ce^{3+} and smaller and more numerous vacancy clusters. This affects charge transfer and H-coupling processes, that play an important role in boosting the rate of H_2 production. The behavior is found to be only slightly dependent on the starting ceria-zirconia composition and it is related to the development of a similar surface hetero-structure configuration, characterized by the presence of at least a ceria-rich solid solution and a (cerium-doped) zirconyl oxynitride phase, which is supposed to act as a promoter for TWS reaction. The above findings confirm the importance of a multi-phase structure in the design of ceria-zirconia oxides for water splitting reaction and allow a step forward to find an optimal composition. Moreover, the results indicate that doping with nitrogen might be a novel approach for the design of robust, thermally resistant and redox active materials.

58 INTRODUCTION

59 The necessity to increase the sustainability of the modern societies requires the development of a
60 circular economy based on an increasing use of renewable resources for the production of energy
61 services. Solar energy and water are winner ingredients for improvement of the energy conversion
62 chain, which would be based on the use of hydrogen or bio-fuels. Among the technologies that exploit
63 the sunlight to produce energy and fuels, solar thermochemical processes have a good potentiality in
64 terms of efficiency and there are excellent reviews that summarize the main outcomes in the field.¹⁻³
65 In these processes the solar resource is used directly to drive endothermic chemical reactions such as
66 the splitting of water (WS) and/or of CO₂ (CDS). Water spontaneously decomposes into elementary
67 O₂ and H₂ only at temperature higher than 3800 °C.³ This condition, along with the necessity of
68 separating O₂ from H₂ makes the direct thermolysis of water impractical. However, the reaction is
69 possible through multi-steps thermal cycles using specific compounds as promoters. Reducible metal
70 oxide redox couples such as SnO₂/SnO, ZnO/Zn, Fe₃O₄/FeO, CeO₂/Ce₂O₃ have been shown suitable
71 to split water in two steps: an endothermic step at high temperature (~1200-2000 °C) in which the
72 oxide is reduced in inert atmosphere and a subsequent exothermic step at lower temperature in which
73 water oxidizes the metal oxide producing H₂ (~400-1300 °C).³ The working temperature of each step,
74 O₂ and H₂ yields, and the fuel purity strongly depend on the type of metal oxide involved. Among
75 many metal oxides proposed in literature, ceria is one of the most promising candidates.⁴ CeO₂ can
76 be reduced to Ce₂O₃⁵ or to CeO_{2-δ} (reaction 1)^{4,6} with the aid of solar energy in an inert atmosphere
77 and at high temperature (1300-1800 °C). Then it can be promptly oxidized by water (reaction 2) at
78 intermediate temperature (500-800 °C) producing pure H₂ on demand without purification, storage
79 and transport complications, as conversely encountered in other metal oxide based cycles.



82 Thermodynamic studies of this cycle suggest that solar to fuels efficiency approaching 30% could be
83 achievable, when a complete heat recovery is accomplished.^{7,8} Several experimental and theoretical
84 studies have identified in the reduction step the main limits of ceria based cycles.^{3,9} At a temperature
85 higher than 1800 °C, which is necessary for a full reduction of CeO₂ to Ce₂O₃, CeO₂ starts to
86 sublime, consequently the yield of cycles has been observed to decrease over the time. At lower
87 temperatures ceria cannot be fully reduced and H₂ production depends on the degree of reduction
88 achieved. Therefore, many studies on ceria-based systems have been focused on decreasing the
89 reduction temperature of the Ce⁴⁺/Ce³⁺ redox couple, while maintaining the high reactivity of reduced
90 Ce³⁺ species towards water.^{3,10} The addition of Zr⁴⁺ into the ceria lattice resulted effective in
91 increasing the thermodynamic driving force of CeO₂ reduction at lower temperatures^{11,12}, while
92 aliovalent dopants have been found less effective.^{13,14} New synthesis strategies to control the
93 morphology and the sintering processes of ceria have also been adopted with success.¹⁵ Most recently
94 other solutions allowed to obtain a high and stable production of H₂, such as the addition of rhodium
95 to ceria lattice as catalyst¹⁶ or the use of a composite of CeO₂ and SnO₂ that under reducing conditions
96 forms a stoichiometric pyrochlore phase more reactive than the non-stoichiometric CeO_{2-δ}.¹⁷
97 The effect of zirconium content in the two steps water splitting reaction has been widely studied^{13,18-}
98 ²¹; a linear increase of the reduction yields as a function of zirconium content was observed up to a
99 content of 25 mol%, while at higher contents a stabilization of the released O₂ was recorded. On the
100 other hand, ceria-zirconia based materials showed a slow kinetics of oxidation.^{3,13,21} The oxidation
101 rate seems to be controlled by intergranular gas-phase diffusion in the material layer. In this case,
102 improving morphological and textural properties of the mixed oxides via co-doping²² or by using
103 different synthesis approaches^{13,23} resulted beneficial due to the possibility of tuning the crystalline
104 size, porosity structure and composition at the nanoscale.²⁴ Most of the research has been focused on
105 ceria rich compositions, which were supposed to be structurally stable to the high temperatures
106 adopted in the reduction step and the attention of scientists was mainly drawn on kinetic and
107 thermodynamic issues of the cycle. Only a few studies investigated the correlations between water

108 splitting performance and structural/compositional modification undergone during the redox
109 steps,^{23,25} despite it is well known that the redox properties of the materials are markedly affected by
110 the thermal and redox history.²⁶ In a recent communication, we showed that also zirconia-rich ceria-
111 zirconia mixed oxides can be suitable for the WS process.²⁷ In that study, it appeared clear that phase
112 segregation and nitridation processes, which were induced by the thermal redox cycles, might play a
113 major role in determining the high activity. The present study investigates in more detail the WS
114 behavior of $\text{Ce}_{0.85}\text{Zr}_{0.15}\text{O}_2$ over more cycles and compares the results with previous outcomes with
115 the aim to find some commonalities governing the overall behavior of ceria-zirconia in
116 thermochemical water splitting reactions. Through the use of positron annihilation life time
117 spectroscopy (PALS) and other complementary techniques we are able to describe for the first time,
118 not only the characteristics of phases but also the arrangement of defects on the surface of material
119 when treated at high temperature under air or nitrogen-containing atmospheres. This allows to put
120 forward a conceivable mechanism that explains the significance of nitridation in the WS activity of
121 ceria-zirconia oxides.

122 **EXPERIMENTAL**

123 **Materials.** $\text{Ce}_{0.85}\text{Zr}_{0.15}\text{O}_2$ was prepared with a surfactant assisted precipitation method as
124 reported elsewhere.²⁸ Briefly, proper amounts of $\text{Ce}(\text{NO}_3)_3 \cdot 6\text{H}_2\text{O}$ salt (Treibacher Industrie AG) and
125 $\text{ZrO}(\text{NO}_3)_2$ liquid gel (Treibacher Industrie AG) were dissolved in demineralized water obtaining a
126 0.2 M solution; concentrated H_2O_2 (35% Sigma-Aldrich) was then added according to the molar ratio
127 $[\text{H}_2\text{O}_2]/[\text{tot metals ions}]$ equal to 3. After 45min of continuous stirring at ambient temperature
128 concentrated $\text{NH}_3 \cdot \text{H}_2\text{O}$ (28% Sigma-Aldrich) was added to obtain a pH value of 10.5. Finally, lauric
129 acid (Sigma-Aldrich), using a molar ratio ($[\text{tot metal ions}]/[\text{lauric acid}]$) equal to 0.25, was directly
130 added and maintained under continuous stirring for 4h. The precipitate was then filtered and washed
131 three times with 0.5L of de-mineralized water and the resulting cake was dried at 100 °C overnight.
132 The dry precipitate was calcined in air at 500 °C for 4h. This method allows to obtain highly

133 homogeneous starting materials, which ensures a reproducible phase segregation. In order to simulate
134 the aging effect undergone during the strongly endothermic step of TWS cycle, the oxide was treated
135 at 1300 °C in nitrogen or air for four hours. Other thermal treatment in air were made at 800 °C/4h,
136 and at 1100 °C. All the samples were cooled down in the atmosphere of treatment and exposed to air
137 at room temperature before of the reactivity tests.

138

139 **Reactivity tests.** The experimental conditions have been chosen on the basis of previous
140 studies.^{20,23} The activity of $\text{Ce}_{0.85}\text{Zr}_{0.15}\text{O}_2$, calcined at 1300 °C/4h either in N_2 (CZ85_ N_2) or in air
141 (CZ85_ air) was evaluated towards a two steps water splitting thermal cycle using two different setups.
142 Reduction degree of the material in N_2 /air atmosphere was measured in a thermogravimetric analyser
143 (Q600-TA Instruments). The thermally aged samples (25mg) were heated at 10°C/min in N_2 flow
144 (100 ml/min) up to 1300°C. The oxygen released from the oxide was evaluated from the weight loss
145 observed during 80 minutes of isotherm at 1300 °C. The water splitting (WS) activity was evaluated
146 in a Micromeritics apparatus using the same method as described by Pappacena et.al.²⁷ Each sample
147 (50 mg) was previously reduced to obtain the same reduction degree achieved in the first endothermic
148 step by using a 5% H_2 /Ar flow and a heating ramp of 10 °C/min up to 700 °C. These conditions have
149 been established through a thermogravimetry analysis (TGA, Q500-TA Instruments) in 5% H_2 /Ar
150 flow by reducing the sample up to 900 °C. The reduced sample was evacuated in He and oxidized by
151 20 pulses of water vapor (30% in Ar flow) at 800 °C. H_2 consumption and production were monitored
152 with a thermal conductivity detector; the total H_2 production was measured by calculating the H_2
153 outcome from the first twenty water vapor pulses. At the end of the WS reaction the sample was
154 oxidized with air for 10min to complete the oxidation and cooled down to ambient temperature in He
155 atmosphere. The cycle was repeated six times. The same experiment was carried out also without
156 completing the oxidation with air in order to verify whether the oxidation conditions may affect the
157 reaction of water splitting.

158 **Characterization.** Structural and surface properties of all materials were investigated through
159 the use of several techniques. X-ray Diffraction analysis (XRD) were performed using a Philips
160 X'Pert diffractometer operated at 40 kV and 40 mA equipped with a nickel-filtered $\text{CuK}\alpha$ radiation.
161 All spectra were collected using a step size of 0.02 2θ degrees and a counting time of 40s per angular
162 abscissa in the range of 20–145 2θ degrees. The Philips X'Pert HighScore software was used for
163 phases identification. The mean crystalline size was estimated from the full width at the half
164 maximum (FWHM) of the X-ray diffraction peaks using the Scherrer's equation²⁹ corrected for the
165 instrument line broadening. Rietveld refinement of XRD spectra was performed by means of
166 GSASEXPGUI program.^{30,31}

167 Raman spectra have been recorded with a LABRAM HR800 equipped with a solid-state laser (Laser
168 XTRA, Toptica Photonics) operating at 785 nm and a Peltier cooled CCD detector. The laser radiation
169 was filtered by an interference filter and was focused on the sample through an Olympus BX41
170 microscope. A 50X Olympus objective (NA = 0.75) has been used. The Rayleigh radiation was
171 rejected using Notch filters. In order to ascertain the absence of artifacts the spectra have been
172 obtained also using excitation radiations, at 512 and 633 nm and two different grids (600 lines/mm;
173 1800 lines/mm).

174 High resolution transmission electron microscopy (HRTEM) was accomplished with a JEOL J2010F
175 instrument equipped with a field emission electron source and operated at 200 kV. Samples were
176 dispersed in alcohol and a drop of the suspension was placed over a grid with holey-carbon film.

177 Specific surface area (SA) and porosity of oxides were measured by nitrogen adsorption/desorption
178 isotherms at 77 K, following the BET and BJH method respectively³², using a Tristar 3000 gas
179 adsorption analyzer (Micromeritics). The pore size distribution was calculated from the desorption
180 branch of the isotherm.

181 XPS was used as the main tool to assess the surface chemical composition of the samples before and
182 after the catalytic process. Analyses were performed on a Perkin-Elmer Φ 5600-ci spectrometer using

183 non-monochromatized Al K α radiation (1486.6 eV). The spectrometer was calibrated by assuming
184 the binding energy (BE) of the Au 4f $_{7/2}$ line at 83.9 eV with respect to the Fermi level. The standard
185 deviation for the BEs values was ± 0.2 eV. Survey scans were obtained in the 0–1300 eV range (187.8
186 eV pass energy, 0.4 eV step $^{-1}$, 0.05 sec step $^{-1}$). Detailed scans were recorded for the C1s, O1s, Zr3d
187 and Ce3d and N1s regions (23.5 eV pass energy, 0.1 eV step $^{-1}$, 0.1 sec step $^{-1}$). The BE shifts were
188 corrected by assigning to the C1s peak associated with adventitious hydrocarbons a value of 284.8
189 eV.³³ The analysis involved Shirley-type background subtraction, non-linear least-squares curve
190 fitting adopting Gaussian-Lorentzian peak shapes, and peak area determination by integration.³⁴ The
191 atomic compositions were evaluated from peak areas using sensitivity factors supplied by Perkin-
192 Elmer, taking into account the geometric configuration of the apparatus.³⁵ The experimental
193 uncertainty on the reported atomic composition values does not exceed $\pm 5\%$.

194 Positron annihilation lifetime spectroscopy experiments (PALS) were carried out with a fast-slow
195 coincidence system which has a resolution of 230ps. The scintillation detectors are plastic scintillator
196 coupled with photomultiplier tubes. A 40 μ Ci 22 Na source of positron was sandwiched between two
197 pieces of identical samples. For each spectrum about 2×10^6 coincidence counts have been recorded
198 to ensure the repeatability of the measurements. The positron lifetime data were analyzed by the
199 lifetime9 program with the necessary source corrections.

200

201 **RESULTS**

202 **Reactivity results.** The endothermic step corresponding to the thermal reduction was
203 evaluated via thermogravimetry by measuring the weight loss of the sample treated at 1300 °C in
204 N $_2$ or air. O $_2$ released during the thermal treatment was 276 μ mol/g and 169 μ mol/g respectively for
205 the sample aged in N $_2$ and air, which corresponds to a degree of Ce $^{4+}$ reduction of 21 mol% and 13
206 mol%. Similar results were reported in literature, but generally using higher temperature.^{19,20}
207 Figure 1 shows the results obtained in the exothermic water splitting experiment for both the N $_2$ -
208 treated oxide and for the sample aged in air. A total of 6 cycles are reported, and the detail for one

209 cycle is shown to the right of the image. N₂-treated sample is more active, and the H₂ production
 210 increases significantly up to a stable value obtained with the fourth cycle. A comparison with results
 211 obtained on Ce_{0.15}Zr_{0.85}O₂ indicates that regardless of initial composition H₂ yields reach close values
 212 for the two nitrogen-pretreated compositions after a few cycles.²⁷ To exclude the role of oxygen in
 213 the promotion of H₂ production observed from the 2nd cycle, the same experiment was repeated
 214 without oxidizing the samples with air at the end of each cycle, and the results are compared in Figure
 215 S1.

216 **Characterization results.** Table 1 summarizes the textural and morphological properties of
 217 Ce_{0.85}Zr_{0.15}O₂ after thermal treatment in the range of temperatures 500-1300 °C. The material shows
 218 a good thermal stability up to 800 °C; higher temperatures causes a large drop in surface area with
 219 values close to 1 m²/g after calcination at 1300 °C, regardless of the gas type used in the treatment.
 220 Correspondingly, an increase of average crystallite size up to 40 nm with loss of porosity is found.
 221 The structure of the samples was investigated at the nanoscale through XRD, Raman spectroscopy
 222 and HRTEM.

223
 224 **Table 1:** Characteristics of Ce_{0.85}Zr_{0.15}O₂ after the thermal treatments.

Calcination Temperature (°C)	Treatment Atmosphere	Specific Surface Area (m ² /g) ^a	Pore size (Å)	Crystallite size (Å) ^b
500	Air	94	238	54
800	Air	45	345	99
1100	Air	9	ND	275
1300	Air	1	ND	425
1300	Nitrogen	1	ND	403

225 a: according to BET method; b: determined with Sherrer equation from XRD analysis., ND: not determined

226
 227 Figure 2 shows the corresponding X-ray diffraction profiles of the samples. After calcination at
 228 500°C the sample crystallizes in a cubic fluorite structure with a unit cell value of 5.3652(5) Å. This
 229 value is lower than the one measured for a pure ceria sample, 5.4118(1) Å, and indicative of the
 230 insertion of Zr⁴⁺ into the ceria lattice. The application of Vegard law³⁶ allows us to calculate a molar
 231 doping of zirconium equal to 0.167, that is very close to the nominal composition of the starting

232 material. No large differences exist among the XRD profiles except for the narrowing of the peaks
233 with the increase of the calcination temperature, indicating sintering of crystallites as a consequence
234 of the thermal treatments.³⁷ However, a careful evaluation of the profiles of samples treated at 1300°C
235 in both air and nitrogen evidences a tiny shift ($2\theta=0.12\pm 0.4$) of the most intense peak (111) of CZ85
236 to higher angles and a small shoulder at $2\theta=28.10$ degrees; thus indicating the occurrence of phase
237 segregation accompanied by small changes in the composition of the cubic CZ85 phase. The small
238 peak at $2\theta=28.10$ is attributable to the presence of a monoclinic zirconia-rich phase, ($\text{Ce}_{0.05}\text{Zr}_{0.95}\text{O}_2$,
239 PDF 88-2392). The XRD profile of the samples sintered in air shows also a small peak at $2\theta=29.83$
240 which is probably related to a tetragonal zirconia-rich phase ($\text{Ce}_{0.18}\text{Zr}_{0.82}\text{O}_2$, PDF 80-0785) or to
241 tetragonal ZrO_2 (JCPDS 01-080-0785). Such type of segregation is consistent with what is reported
242 in literature for similar compositions.³⁸

243 Figure 3 shows the Raman spectra of samples treated at 1300 °C before and after WS cycles. Figure
244 S2 shows also the spectra collected using excitation lines at 512 and 633 nm. Spectra in the region
245 $180\text{-}800\text{ cm}^{-1}$ are characterized by an intense signal at ca. 476 cm^{-1} corresponding to the fundamental
246 vibration mode F_{2g} of the fluorite structure and satellite bands at 300 and 602 cm^{-1} , consistent with a
247 distortion of the cubic structure and the presence of a tetragonal t'' phase.³⁹ The minority phases are
248 not detectable and the spectra of the samples before and after WS cycles are almost identical. Above
249 1000 cm^{-1} all the spectra show complex bands which are generally attributable to electronic f-f
250 transitions of Ln^{3+} ions present as impurities in the materials.³⁸ Alternatively, these bands have been
251 also associated to the presence of Ce^{3+} ions.^{39,41,42} It is interesting to note that the intensity of these
252 bands, which is generally related to the asymmetry of the sites, increases after the cycles.

253 Figure 4A shows a HRTEM image of the sample treated in nitrogen at high temperature. The
254 crystallite labeled “a” corresponds to a single cubic CZ particle oriented along the [110]
255 crystallographic direction. Spots at 3.0 \AA correspond to the cubic (111) planes. In contrast, the
256 crystallite labeled “b” shows a FT pattern exhibiting spots aligned at 2.5 and 5.1 \AA as well as spots at

257 2.9 Å. The spots aligned at 2.5 and 5.1 Å are ascribed to the (400) and (200) crystallographic planes
258 of Zr₂ON₂, respectively, whereas those at 2.9 Å correspond to the (222) planes of Zr₂ON₂.
259 These results are in good agreement with those reported in literature⁴², except for tiny differences
260 which could be explained with the insertion of cerium in the structure. This hypothesis is reasonable
261 considering that Ce³⁺ (103 pm) has an effective ionic radius similar to that of La³⁺, and that the
262 formation of LaZrO₂N has been demonstrated.⁴⁴ The HRTEM analysis of sample treated in air (Figure
263 4B) does not evidence the presence of the oxynitride phase. FT image with spots at 3.0 Å corresponds
264 to the (111) planes of cubic CZ, which is the dominant phase. The effects of WS cycles at the
265 nanoscale are shown in Figure 4C. The TEM image (left) evidences a sample constituted by
266 crystallites measuring more than 100 nm in a compact arrangement, suggesting that the sample
267 sintered during the cycles. Triple junctions are easily recognized, which usually appear upon high
268 temperature calcination treatments. The figure at the right corresponds to a representative HRTEM
269 image of the sample. In this case, only lattice fringes corresponding to the CZ oxide are recognized.
270 In the figure, several lattice fringes are indicated and correspond to the (111), (220) and (222)
271 crystallographic planes of cubic CZ at 3.0, 1.8 and 1.5 Å, respectively.
272 The composition and defects structure of samples before and after WS cycles are investigated through
273 XPS and PALS techniques. Figures 5A and B show the XPS spectra and the corresponding fitting
274 components of Ce3d and O1s regions for the samples treated at 1300 °C in nitrogen. Similar features
275 were observed for the air-treated sample and for the samples after six WS cycles (see Figure S3 and
276 S4). Figures 5C and D show the N1s region of the sample treated in nitrogen before and after WS
277 cycles.
278 In Figure 5A, U and V refer to cerium 3d_{3/2} and 3d_{5/2} spin-orbit components, respectively. U, U'', U''',
279 V, V'', and V''' refer to the final states of Ce⁴⁺, while U°, U' and V°, V' refer to those of Ce³⁺ [25].
280 The fitted peak areas were used to estimate the relative amount of Ce³⁺ and Ce⁴⁺ (see Table 2). The
281 O1s region is suitably fitted with two components (Figure 5B). The main component (peak 1) at about
282 529.5 eV is associated with the cerium–zirconium oxide matrix, while the component centered at

283 531.5 eV (peak 2) can be ascribable mainly to surface hydroxyl groups.⁴⁴ The signal N1s at 399.9 eV
284 (Figure 5C) confirmed the insertion of nitrogen into the surface of the CZ85_N₂ and the formation of
285 a zirconyl oxynitride phase^{27,46,47} In addition, the evidence of the same nitrogen peak on the CZ85_N₂
286 surface after WS cycles (CZ85_N₂_ws, Figures 5D) indicates that the oxynitride phase is stable under
287 WS conditions. No signal corresponding to insertion of nitrogen is observed for samples treated under
288 air.

289 Table 2 summarizes the surface chemical composition (atomic %) of the samples, determined from
290 the analysis of Ce3d and Zr3d XPS peaks.

291 Sample calcined at 500 and 1100 °C show a surface composition consistent with the nominal
292 stoichiometry of the Ce_{0.85}Zr_{0.15}O₂ solid solution revealing that the starting material was
293 homogeneous and thermally stable up to 1100 °C. After treatment at 1300 °C the value of Zr/Ce ratio
294 increase to 0.26 in agreement with the phase segregation observed by XRD and indicating that
295 zirconia-rich compositions are mainly located on the outer part of the crystallite. The presence of Ce³⁺
296 in the starting material (500 °C) is due to the nanometric nature of the powder and to the presence of
297 extrinsic defects induced by the zirconium doping.³⁸ Besides, a small quantity of Ce³⁺ could be
298 generated by the reduction of Ce⁴⁺ under the X-ray irradiation during XPS analysis.⁴⁸ The amount of
299 Ce³⁺ increased after calcination at 1100 and 1300 °C as expected from the state diagrams of CeO₂ in
300 air and N₂ conditions, for which CeO₂ starts reducing above 1000 °C.^{4,6} After water splitting cycles
301 the concentration of Ce³⁺ remained the same for the sample treated in nitrogen, while it slightly
302 decreased in the case of the sample pretreated in air. For the N₂ treated sample the extent of surface
303 nitridation, was determined from the N/Ce atomic ratio which resulted similar before and after the
304 WS reaction, with a value of ca. 0.03. However, due to the very low intensity of the N1s peak, this is
305 only a rough estimate.

306

307 Table 2. Results of XPS analysis

Sample	Ce ^b [Ce ³⁺ , Ce ⁴⁺] ^c	Zr ^b	Zr/Ce	Ce ³⁺ /Ce ⁴⁺
CZ85-500 ^a	84.2 [14.3, 69.9]	15.8	0.19	0.20
CZ85-1100 ^a	85.4 [22.2, 63.2]	14.6	0.17	0.35
CZ85_air	79.0 [22.1, 56.9]	21.0	0.26	0.39
CZ85_N2	79.1 [24.5, 54.6]	20.9	0.26	0.45
CZ85_air_WS	79.8 [18.4, 61.4]	20.2	0.26	0.30
CZ85_N2_WS	79.1 [24.5, 54.6]	20.9	0.26	0.45

308 a - the number indicates the temperature of calcination in air; b-the uncertainty on the quantitative values does not exceed
309 $\pm 5\%$, c - values obtained from fitting of the Ce3d region.
310

311 Details into the organization of surface defects were obtained via positron annihilation lifetime
312 spectroscopy (PALS). Figure S5 shows the PALS spectra for some representative sample. All spectra
313 were fitting to three lifetime components (τ_1 , τ_2 , τ_3) and the corresponding values along with their
314 relative intensity (I_1 , I_2 , I_3) are summarized in Table 3. As far as we know, this is the first time that
315 PALS technique is applied to the characterization of CZ85 mixed oxides, therefore we used a CZ85
316 sample calcined at 1100 °C as a reference material for an interpretation of the data. Since the
317 temperature used for treatment is not enough high to cause phase segregation and thermal reduction,
318 such a sample is representative of a homogeneous highly sintered composition.

319 The longest component τ_3 is attributed to the annihilation of orthopositronium atoms formed in the
320 large voids present in the material.⁴⁹ It hardly helps in giving some useful information of defects in
321 the samples because the formation of the orthopositronium atoms are not related to the positron
322 trapping at defects, so it will be neglected in the following discussion. The component τ_1 is generally
323 attributed to the free annihilation of positrons in defect-free crystal. However, for disordered systems
324 it may also be associated to small defects (like mono vacancies) and shallow positrons traps (like
325 oxygen vacancies), which can decrease the average electron density and elongation of τ_1 .^{50,51}

Table 3: Peak-fitting results of PALS spectra, Spectra fitted with the Lifetime9 software.

sample	τ_1 (ps)	τ_2 (ps)	τ_3 (ns)	I_1 (%)	I_2 (%)	I_3 (%)
CZ85_air	170.8	310.0	1.09	78.9	20.8	0.35
CZ85_N₂	175.2	358.0	1.02	72.2	26.6	1.20
CZ85_N₂_ws	173.7	351	1.83	83.9	15.5	0.53
CZ85_air_ws	164.4	291	1.4	74.6	25.0	0.44
CZ85-1100	179.1	359	0.95	47.2	51.9	0.88

326

327 In many studies on ceria based oxides in form of nano-powders, this first component τ_1 has been
 328 related to neutral oxygen mono-vacancies associated to Ce^{3+} ($Ce'_{ce}V_{\bullet\bullet}O_{ce}$) according to Kröger
 329 and Vink's defect notation).⁵² From Table 3 we can see the τ_1 values are about ~175 ps, which are far
 330 lower than that reported in literature, indicating that the small vacancies have higher electron density
 331 in our samples. Such a difference might be due to the fact that, in our case, the material has a larger
 332 crystal size owing to its sintering at high temperature.⁵¹ The component τ_2 is much larger than the
 333 component τ_1 , and it arises from positrons trapped by larger size defects. These type of defects mainly
 334 locate on the surface or subsurface, thus τ_2 should give useful information on the surface defects of
 335 samples.^{52,54}

336 It is worth noting that the values of τ_1 and τ_2 for the reference sample CZ85-1100 are very similar to
 337 the respective life times for the sample treated in nitrogen before the test (CZ85_N₂). Conversely, the
 338 related intensity I_1 and I_2 are different, the thermal treatment in nitrogen leads to a decrease of the
 339 number of large size clusters on the surface with respect to the reference. The sample treated in air
 340 (CZ85_air) shows a lower value of τ_2 . Taking into account that the electron density is lower in the
 341 large size clusters rather than in the small defects, and consequently the positron lifetime increases in
 342 the larger size defects, it is inferred that in the air-treated sample the clusters of defects are smaller
 343 than in the N₂-treated sample or in the reference. Moreover, by comparing the ratio I_1/I_2 of the two

344 samples heated at 1300 °C, it is clear that the material treated in nitrogen have a higher clusters density
345 than that treated in air.

346 After WS cycles, both the samples treated in nitrogen and that treated in air showed lower values of
347 τ_1 and τ_2 . The entity of the decrease is more significant for the sample treated in air (CZ85_air_ws)
348 rather than for the sample treated in nitrogen (CZ85_N₂_ws). Opposite trends have been observed for
349 the value of I_2 in the two samples. After cycles the value of I_2 diminished of the 37% for the
350 CZ85_N₂_ws, while increased 20% for the CZ85_air_ws. That implies respectively a less or higher
351 number of defects clusters in the two samples after reaction.

352 **DISCUSSION**

353 The results indicate that thermal treatment either in N₂ or air at high temperature of Ce_{0.85}Zr_{0.15}O₂
354 induces subtle structural changes promoting phase segregation. The material treated under nitrogen
355 shows the formation of a zirconia based oxy-nitride phase located at the outer part of the grains that
356 is beneficial for the water splitting reaction. The active phase is composed by this oxynitride phase
357 which is present in catalytic amount and by a pseudo-cubic oxide rich in ceria (Ce_xZr_{1-x}O_{2- δ} , 0.7 \leq x \leq
358 0.9) as a major phase. This study uses XPS and PALS to obtain more details into the defects
359 organization of these heterogeneous structures to see how the structure and quantity of oxygen
360 vacancies can help in developing more stable and robust WS catalysts.

361 In agreement with previous observations, our findings confirmed that the main surface defects in
362 ceria–zirconia oxide are polarons, which are related to Ce³⁺ centers, and oxygen vacancies.⁵⁵ XPS
363 analysis accounts for the number of Ce³⁺ (Table 2) while PALS technique gives information on the
364 organization of oxygen vacancies (Table 3). The material treated in nitrogen shows a higher
365 concentration of Ce³⁺ and larger oxygen vacancy clusters at its surface in comparison to the sample
366 treated in air. Moreover, the configuration of these defects remains almost the same after redox cycles
367 (the same amount of Ce³⁺ and the same dimensions of cluster, even if clusters number decreased).
368 Conversely, the sample treated under air shows a new arrangement of defects with the presence of

369 smaller and more numerous vacancy clusters and a decreased amount of Ce^{3+} at the surface. Since
370 the thermal treatments in nitrogen or air caused similar structural and compositional changes in the
371 oxide material, the different configuration of vacancies in air and N_2 treated materials has to be related
372 with the nitridation process and the initial reduction degree of the two materials. Assuming that charge
373 neutrality has to be preserved, the substitution of O^{2-} anions with N^{3-} must be balanced by the
374 introduction of oxygen vacancies.⁵⁶ The addition of these extra vacancies along with the necessary
375 vacancies to balance Ce^{3+} charges, (more numerous in the sample treated in nitrogen because more
376 reduced) may justify the formation of larger vacancy clusters in the sample treated in nitrogen.
377 Defects configurations after testing are related to samples oxidized with water, and the differences
378 observed for the two materials suggest that water splitting proceeded through different pathways. We
379 can put forward some hypotheses on basis of recent theoretical and experimental studies regarding
380 the stability and behavior of reduced $\text{CeO}_2(111)$ surface when interacting with water.⁵⁷ It is reported
381 that large surface vacancy clusters are formed and stabilized via a “hydroxyl-vacancies model”.⁵⁸ The
382 coexistence of hydroxyl groups and vacancies at the subsurface of $\text{CeO}_{2-x}(111)$ favors the stabilization
383 of vacancy dimers or trimers at the surface. Large clusters at the surface in turns favor the mobility
384 of H in the bulk and a higher concentration of Ce^{3+} at the surface.⁵⁹ The formation and presence of
385 subsurface hydroxyl groups favor the H transfer between neighboring top-surface O and subsurface
386 O rather than the direct surface diffusion of H among top surface O, because of the lower energy
387 barrier of the mechanism.⁵⁸ The high concentration of Ce^{3+} at the surface, close to vacancy clusters
388 leads to a more significant charge modification of the neighboring surface O pushing more covalent
389 electrons towards O. This would contribute to weaken the H-O bond and, consequently, benefit the
390 process of H coupling, which requires O-H bond breaking, to form H_2 .

391 The water splitting process involves surface reactions (i.e. adsorption/dissociation of water,
392 ion/electron transfer on the surface and association of H atoms and H_2 desorption), and incorporation
393 of ions into the bulk. Recently it has been demonstrated that in ceria-zirconia based materials the
394 surface oxygen-ions transfer, mediated by bulk oxygen vacancies is fast and that the rate determining

395 step of reaction is related to the reduction of hydroxyl groups, and to the release of H₂, rather than
396 due to the incorporation of ions into the bulk.^{60,55}

397 Our results agree with the idea illustrated in Figure 6. The oxynitride phase contributes to create and
398 stabilize large vacancy oxygen clusters⁶¹ that at the first cycle can be easily hydroxylated (Figure 6
399 A-C). The co-existence of these large clusters and hydroxyl groups helps maintaining reduced surface
400 through a rapid replacement of vacancies from the bulk and an incorporation of hydroxyl groups into
401 the subsurface layers of the oxide (Figure 6 D). This configuration contributes to boost the rate
402 determining step of water splitting to produce H₂, thus explaining the higher reactivity of the material
403 treated in N₂ from the second cycle. In this view, the material treated under air lacks of suitable centers
404 to induce hydroxylation of subsurface and the reaction will be limited at the surface with a less
405 effective rearrangement of defects over cycles.

406 This study allows also to clarify and explain the behavior of Zr-rich compositions like Ce_{0.15}Zr_{0.85}O₂.²⁷
407 Despite this latter composition is less thermally stable and shows a more significant surface
408 segregation under nitrogen flow, the final composition at the outer part of the particles is similar to
409 that observed for Ce_{0.85}Zr_{0.15}O₂. Figure 7 summarizes the main steps of the transformation for both
410 compositions trying to elucidate the reasons why ceria-rich and zirconia-rich materials show similar
411 water splitting reactivity after thermal treatment in nitrogen and redox activation. It is worth noting
412 that after thermal treatment we end up with a surface phase arrangement which is characterized by
413 the co-presence of Ce_xZr_{1-x}O_{2-δ}, 0.7 ≤ x ≤ 0.9 and Zr₂ON₂, which is formed from the nitridation of
414 segregated zirconia and is stable under redox cycles. The possibility that under our conditions the
415 oxynitride phase might be doped with cerium cannot be excluded, and further investigations are
416 requested to better address the nitridation mechanism and the stability of such phases.

417

418 **CONCLUSIONS**

419 This study investigates the structural changes occurring on $\text{Ce}_{0.85}\text{Zr}_{0.15}\text{O}_2$ during thermochemical
420 water splitting cycles. It is found that thermal aging in nitrogen atmosphere modifies the surface
421 structure and composition of the materials by promoting the segregation of a ceria-zirconia solid
422 solution rich in ceria along with a zirconia-oxynitride phase, a fate that is similar to that found over
423 zirconia-rich compositions. Positron Annihilation Lifetime Spectroscopy measurements have shown
424 that the oxynitride phase contributes to form large surface vacancy clusters with an appropriate defect
425 configuration which promotes charge transfer and H coupling, thus playing a pivotal role in boosting
426 the production of H_2 . Modification in the size distribution and number of structural defects can
427 explain the different behavior when the material is treated under air atmosphere.

428 All these findings suggest new approaches for the development and design of ceria based materials
429 for the two-step water splitting reaction and highlight the importance of engineering the surface defect
430 structure/configuration of the material to obtain an efficient catalyst. In this regard, the role and the
431 impact of nitridation process need to be further investigated.

432

433 **ASSOCIATED CONTENT**

434 **Supporting Information**

435 Reactivity test, Raman spectra, XPS, HRTEM, PALS spectra

436 **AUTHOR INFORMATION**

437 **Corresponding Author**

438 * E-mail: marta.boaro@uniud.it. Tel.:(+39)0432-558825. Fax (+39)0432-558803

439

440 **REFERENCES**

441 (1) Miller, J.E.; McDaniel, A.H.; Allendorf, M.D. Considerations in the Design of Materials for Solar-
442 Driven Fuel Production Using Metal-Oxide Thermochemical Cycles. *Adv. Energy Mater.* **2014**, *4*, 1-
443 19.

444 (2) Agrafiotis, C.; Roeb M.; Sattler, C.A Review on Solar Thermal Syngas Production via Redox
445 Pair-Based Water/Carbon Dioxide Splitting Thermochemical Cycles. *Ren. Sust. Energy* **2015**, *42*,
446 254-285.

- 447 (3) Scheffe, J.R.; Steinfeld, A. Oxygen Exchange Materials for Solar Thermochemical Splitting of
448 H₂O and CO₂: a review. *Mat. Today* **2014**, *17*, 341-348.
- 449 (4) William, C.C.; Haile, M.S. Thermochemical Study of Ceria: Exploiting and Old Material for New
450 Modes of Energy Conversion and CO₂ Mitigation. *Phil. Trans. R. Soc. A* **2010**, *368*, 3269-3294.
- 451 (5) Abanades, S.; Flamant, G. Thermochemical Hydrogen Production from a Two-Step Solar-Driven
452 Water-Splitting Cycle Based on Cerium Oxides. *SolarEnergy* **2006**, *80*, 1611-1623.
- 453 (6) Chueh, W.C.; Falter, C.; Abbott, M.; Scipio, D.; Furler, P.; Haile, S.M.; Steinfeld, A. High-Flux
454 Solar-Driven Thermochemical Dissociation of CO₂ and H₂O Using non-Stoichiometric Ceria.
455 *Science* **2010**, *330*, 1797-1801.
- 456 (7) Lapp, J.; Davidson, J.H.; Lipiński, W. Efficiency of two-step Solar Thermochemical Non-
457 Stoichiometric Redox Cycles with Heat Recovery. *Energy* **2012**, *37*, 591-600.
- 458 (8) Siegel, N.P.; Miller, J.E.; Ermanoski, I.; Diver, R.B.; Stechel, E.B. Factors Affecting the
459 Efficiency of Solar Driven Metal Oxide Thermochemical Cycles. *Ind. Eng. Chem. Res.* **2013**, *52*,
460 3276-3286.
- 461 (9) Bufin, B.; Call, F.; Lange, M.; Lübben, O.; Sattler, C.; Pitz-Paal, R.; Shvets I.V. Thermodynamics
462 of CeO₂ Thermochemical Fuel Production. *Energy Fuels* **2015**, *29*, 1001-1009.
- 463 (10) Scheffe, J.R.; Steinfeld, A. Thermodynamic Analysis of Cerium-Based Oxides for Solar
464 Thermochemical Fuel Production. *Fuels* **2012**, *26*, 1928-1936.
- 465 (11) Kim, T.; Vohs, J.M.; Gorte, R.J. Thermodynamic Investigation of the Redox Properties of
466 Ceria-Zirconia Solid solutions. *Ind. Eng. Chem. Res.* **2006**, *45*, 5561-5565.
467
- 468 (12) Hao, Y.; Yang, C.-K.; Haile, S.M. Ceria-Zirconia Solid Solutions (Ce_{1-x}Zr_xO_{2-δ}, x ≤ 0.2) for
469 Solar Thermochemical Water Splitting: A Thermodynamic Study. *Chem. Mater.* **2014**, *26*,
470 6073-6082.
- 471
- 472 (13) Le Gal, A.; Abanades, S.; Bion, N.; Le Mercier, T.; Harlé, V. Reactivity of doped Ceria-Based
473 Mixed Oxides for solar Thermochemical Hydrogen generation via Two Step Water Splitting Cycles.
474 *Energy Fuel* **2013**, *27*, 6068-6078.
- 475 (14) Le Gal, A.; Abanades, S. Dopants Incorporation in Ceria for Enhanced Water Splitting: Activity
476 During Solar Thermochemical Hydrogen Generation. *J. Phys. Chem. C* **2012**, *116*, 13516-13523.
- 477 (15) Rudisill, S.G.; Venstrom, L.J.; Petkovich, N.D.; Quan, T.; Hein, N.; Boman, D.B.; Davidson,
478 A.; Stein, J.H. Enhanced Oxidation Kinetics in Thermochemical Cycling of CeO₂ through template
479 porosity. *J. Phys. Chem C* **2013**, *117*, 1692-1700.
- 480 (16) Lin F.J.; Rothensteiner, M.; Alxneit I.; van Bokhoven, J.A.; Wokaun, A. First demonstration of
481 direct hydrocarbon fuel production from water and carbon dioxide by solar-driven thermochemical
482 cycles using rhodium-ceria. *Energy Environ Sci.* **2016**, *9*, 2400-2409.
- 483 (17) Ruan, C.; Tan, Y.; Li, L.; Wang, J.; Liu, X.; Wang, X. A novel CeO_{2-x}SnO₂/Ce₂Sn₂O₇ Pyrochlore
484 Cycles for Enhanced Solar Thermochemical Water Splitting. *AIChE J.*, **2017**. *63*, 3450-3463.

- 485 (18) Kaneko, H.; Taku, S.; Tamaura, T. Reduction Reactivity of CeO₂-ZrO₂ Oxide Under High O₂
486 Partial Pressure in Two-Step Water Splitting Process. *Solar Energy* **2011**, *85*, 2321-2330.
- 487 (19) Le Gal, A.; Abanades, S.; Flamant, G. CO₂ and H₂O Splitting for Thermochemical Production
488 of Solar Fuels using Non-Stoichiometric Ceria and Ceria/Zirconia Solid Solutions. *Energy Fuels*
489 **2011**, *25*, 4836-4845.
- 490 (20) Le Gal, A.; Abanades, S. Catalytic Investigation of Ceria-Zirconia Solid Solutions for Solar
491 Hydrogen Production. *Int. J. Hydrogen Energy* **2011**, *36*, 4739-4748.
- 492 (21) Bulfin, B.; Lange, M.; de Oliveira, L.; Roeb, M.; Sattler, C. Solar Thermochemical Hydrogen
493 Production Using Ceria Zirconia Solid Solutions: Efficiency analysis. *Int. J. Hydrogen Energy* **2016**,
494 *41*, 19320-19328.
- 495 (22) Dasari, H.P.; Ahn, K.; Park, S.-Y.; Ji, H.-I.; Yoon, K.J.; Kim, B.-K.; Je, H.-J.; Lee, H.-W.; Lee,
496 J.-H. Hydrogen Production from Water-Splitting Reaction Based on RE-Doped Ceria-Zirconia
497 Solid-Solutions. *Int. J. Hydrogen Energy* **2011**, *38*, 6097-6103.
498
- 499 (23) Petkovich, N.D.; Rudisill, S.G.; Venstrom, L.J.; Boman, D.B.; Davidson J.H.; Stein, A. Control
500 of Heterogeneity in Nanostructured Ce_{1-x}Zr_xO₂ Binary Oxides for Enhanced Thermal Stability and
501 Water Splitting Activity. *J. Phys. Chem. C*, **2011**, *115*, 21022-21033.
- 502 (24) Wu, K.; Sun, L.-D.; Yan, C.H. Recent Progress in Well-Controlled Synthesis of Ceria-Based
503 Nanocatalysts towards Enhanced Catalytic Performance. *Adv. Energy Mater.* **2016**, *6*, 1-46.
- 504 (25) Pappacena, A.; Boaro, M.; Šolcová, O.; Trovarelli, A. *Trans Tech Publications*, Ceria Based
505 Materials with Enhanced OSC Properties for H₂ Production by Water Splitting Reaction Advances in
506 Science and Technology. **2014**, *93*, 76-81
- 507 (26) Boaro, M.; Desinan, S.; Abate, C.; Ferluga, M.; de Leitenburg, C.; Trovarelli, A. Study on Redox,
508 Structural and Electrical Properties of Ce_xZr_{1-x}O₂ for Applications in SOFC Anodes. *J. Electrochem.*
509 *Soc.* **2011**, *158*, P22-29.
- 510 (27) Pappacena, A.; Boaro, M.; Armelao, L.; Llorca, J.; Trovarelli, A. Water Splitting Reaction on
511 Ce_{0.15}Zr_{0.85}O₂ Driven by Surface Heterogeneity. *Catal. Sci. Technol.* **2016**, *6*, 399-403.
- 512 (28) Pappacena, A.; Scherzanz, K.; Sagar, A.; Aneggi, E.; Trovarelli, A. Development of a Modified
513 Co-Precipitation Route for Thermally Resistant, High Surface Area Ceria-Zirconia Based Solid
514 Solutions *Stud. Surf. Sci. Catal.* **2010**, *175*, 835-838.
- 515 (29) Warren, B.E.; *X-ray Diffraction*; Dover Publications INC: New York, 1990.
- 516 (30) Toby, B. H. J. *Appl. Crystallogr.* **2001**, *34*, 210-213.
- 517 (31) Larson, A. C.; Dreele, R. B. V. *General Structure Analysis System "GSAS"*; Los Alamos
518 National Laboratory: Los Alamos, NM, 2000.
- 519 (32) Lowell, S.; Shields, J.E.; Thomas, M.A.; Thommes, M. *Characterization of Porous Solids and*
520 *Powders: Surface Area, Pore Size and Density*; Kluwer Academic Publisher, Springer: Dordrecht,
521 2006.
- 522 (33) Briggs D.; Seah, M. *In Practical Surface Analysis*; Ed. Wiley: Chichester, 1990.

- 523 (34) Shirley, D.A. High-Resolution X-Ray Photoemission Spectrum of the Valence Bands of Gold.
524 *Phys. Rev. B: Condens. Matter.* **1972**, *5*, 4709-4714.
- 525 (35) Moulder, J.F.; Stickle, W.F.; Sobol, P.E.; Bomben, K.D. *Handbook of X-ray Photoelectron*
526 *Spectroscopy, Physical Electronics*, J. Chastain (Ed.): Eden Prairie, MN, 1992.
- 527 (36) Hong, S.J.; Virkar, A.V. Lattice Parameters and Densities of Rare-Earth Oxide Doped Ceria
528 Electrolytes. *J. Am. Ceram. Soc.* **1995**, *78*, 433-439.
- 529 (37) Zhang, F.; Chen, C.-H.; Hanson, J.C.; Robinson, R.D.; Herman, I.P.; Chan, S.-W. Phases in
530 Ceria-Zirconia Binary Oxide (1-x)CeO₂-xZrO₂ Nanoparticles: the Effect of Particle Size. *J. Am.*
531 *Ceram. Soc.* **2006**, *89*, 1028-1036.
- 532 (38) Prusty, D.; Pathaka, A.; Mukherjee, M.; Mukherjee, B.; Chowdhury, A. TEM and XPS
533 Studies on the Faceted Nanocrystals of Ce_{0.8}Zr_{0.2}O₂. *Mater. Charact.* **2015**, *100*, 31-35.
- 534 (39) Kaspar, J.; Fornasiero, P.; Balducci, G.; Di Monte, R.; Hickey, N.; Sergio, V. Effect of ZrO₂
535 Content on Textural and Structural Properties of CeO₂/ZrO₂ Solid Solutions Made by Citrate
536 Complexation Route. *Inorg. Chim. Acta* **2003**, *349*, 217-226.
- 537 (40) Fornasiero, P.; Speghini, A.; Di Monte, R.; Bettinelli, M.; Kašpar, J.; Bigotto, A.; Sergio, V.;
538 Graziani, M. Laser-Excited Luminescence of Trivalent Lanthanide Impurities and Local Structure in
539 CeO₂-ZrO₂ Mixed Oxides. *M. Chem. Mater.* **2004**, *16*, 1938-1944.
- 540 (41) Sullivan, J.A.; Dulgheru, P.; Atribak, I.; Bueno-López, A.; García-García, A. Attempts at an in
541 Situ Raman Study of Ceria/Zirconia Catalysts in PM Combustion. *Appl. Catal. B: Environ.* **2011**,
542 *108-109*, 134-139.
- 543 (42) Nolas, S.; Tsoukala, V.G.; Gayen, S.K. Electronic-Raman-Scattering Study of the Low-Lying
544 Energy Levels of Trivalent Cerium-Doped Yttria. *Phys. Rev. B* **1994**, *50*, 150-158.
- 545 (43) Füglein, E.; Hock, R.; Lerch, M. Crystal Structure and High Temperature Behavior of Zr₂ON₂.
546 *Z. Anorg. Allg. Chem.* **1997**, *623*, 304.
- 547 (44) Yang, M.; Rodgers, J.A.; Middler, L.C.; Oró-Solé, J.; Jorge, A.B.; Fuertes, A.; Atfield, J.P.
548 Direct Solid-State Synthesis at High Pressures of New Mixed-Metal Oxynitrides: RZrO₂N (R = Pr,
549 Nd, and Sm). *Inorg. Chem.* **2009**, *48*, 11498-11500.
- 550 (45) Nelson, A.E.; Schulz, K.H.; Surface Chemistry and Microstructural Analysis of Ce_xZr_{1-x}O_{2-y}
551 Model Catalyst Surfaces *Appl. Surf. Sci.* **2003**, *210*, 206-221.
- 552 (46) Signore, M.A.; Rizzo, A.; Mirengi, L.; Tangliente, M.A.; Cappello, A.; Characterization of
553 zirconium oxynitride films obtained by radio frequency magnetron reactive sputtering *Thin Solid*
554 *Films* **2007**, *515*, 6798-6804.
- 555 (47) Roman, D.; Bernardi, J.; de Amorim, C.; de Souza, F.; Spinelli, A.; Giacomelli, C.; Figuero, C.;
556 Baumvol, I.; Basso, R. Effect of Deposition Temperature on Microstructure and Corrosion Resistance
557 of ZrN Thin Films Deposited by DC Reactive Magnetron Sputtering. *Mater. Chem. Phys.* **2011**, *130*,
558 147-153.

- 559 (48) Qiu, L.; Liu, F.; Zhao, L.; Ma, Y.; Yao, J. Comparative XPS Study of Surface Reduction for
560 Nanocrystalline and Microcrystalline Ceria Powder. *Appl. Surface Sci.* **2006**, *252*, 4931-4935.
- 561 (49) Chakraverty, S.; Mitra, S.; Mandal, K.; Nambissan, P.M.G.; Chattopadhyay, S. Positron
562 Annihilation Studies of some Anomalous Features of NiFe₂O₄ Nanocrystals Grown in SiO₂. *Phys.*
563 *Rev. B* **2005**, *71*, 024115.
- 564 (50) Dutta, S.; Chattopadhyay, S.; Jana, D.; Banerjee, A.; Manik, S.; Pradhan, S.K.; Sutradhar, M.;
565 Sarkar, A. Annealing Effect on Nano-ZnO Powder Studied from Positron Lifetime and Optical
566 Absorption Spectroscopy. *J. Appl. Physics* **2006**, *100*, 114328.
- 567 (51) Sanyal, D.; Banerjee, D.; De, U. (Bi_{0.92}Pb_{0.17})₂Sr_{1.91}Ca_{2.03}Cu_{3.06}O_{10+δ} Superconductors from 30
568 to 300 K by Positron-Lifetime Measurements. *Phys. Rev. B* **1998**, *58*, 15226.
- 569 (52) Liu, X.; Zhou, K.; Wang, L.; Wang, B.; Li, Y. Oxygen Vacancy Clusters Promoting Reducibility
570 and Activity of Ceria Nanorods. *J. Am. Chem. Soc.* **2009**, *131*, 3140–3141.
- 571 (53) Prochazka, I.; Cizek, J.; Melikhova, O.; Konstantinova, E.T.; Danilenko, I.A.; Yashehisyn, I.
572 A.; Positron Annihilation Study of Zirconia Nanopowders and Nanoceramics Stabilized by Magnesia
573 and Ceria. *J. Am. Ceram. Soc.* **2014**, *97*, 982-989.
- 574 (54) Kong, M.; Li, Y.; Chen, X.; Tian, T.; Fang, P.; Zheng, F.; Zhao, X. Tuning the Relative
575 Concentration Ratio of Bulk Defects to Surface Defects in TiO₂ Nanocrystals Leads to High
576 Photocatalytic Efficiency. *J. Am. Chem. Soc.* **2011**, *133*, 16414-16417.
- 577 (55) Zhao, Z.; Uddi, M.; Tsvetkov, N.; Yildiz, B.; Ghoniem A.F. Redox Kinetics Study of Fuel
578 Reduced Ceria for Chemical-Looping Water Splitting. *J Phys. Chem. C* **2016**, *120*, 16271-16269.
- 579 (56) Lerch, M. Nitridation of Zirconia. *J Am. Ceram. Soc.* **1996**, *79*, 2641-2644.
- 580 (57) Chen, B.; Ma, Y.; Ding, L.; Xu, L.; Wu, Z.; Yuan, Q.; Huang, W. Reactivity of Hydroxyls and
581 Water on a CeO₂(111) Thin Film Surface: The Role of Oxygen Vacancy. *J. Phys. Chem. C.* **2013**,
582 *117*, 5800-5810.
- 583 (58) Wu, X.P.; Gong, X.-Q. Clustering of Oxygen Vacancies at CeO₂(111): Critical Role of
584 Hydroxyls. *Phys. Rev. Lett.* **2016**, *116*, 086102, 1-6.
- 585 (59) Wu, X.P.; Gong, X.-Q.; Lu, G. Role of Oxygen Vacancies in the Surface Evolution of H₂ at
586 CeO₂(111): a Charge Modification Effect. *Phys. Chem. Chem. Phys.* **2015**, *17*, 3544-3549.
- 587 (60) Feng, A.; Galaby, F.E.; Ye, X.; Shen, Z.-X. Chueh, W.C. Fast Vacancy-Mediated Oxygen Ion
588 Incorporation Across the Ceria-Gas Electrochemical Interface. *Nature Comm.* **2014**, *5*, 1-8.
- 589 (61) Attfield, J.P. Principles and Applications of Anion Order in Solid Oxynitrides. *Cryst. Growth*
590 *Des.* **2013**, *13*, 4623-4629.

591

592

593
 594
 595
 596
 597
 598
 599
 600
 601
 602
 603
 604
 605
 606
 607
 608
 609
 610
 611
 612
 613
 614
 615
 616
 617
 618
 619
 620

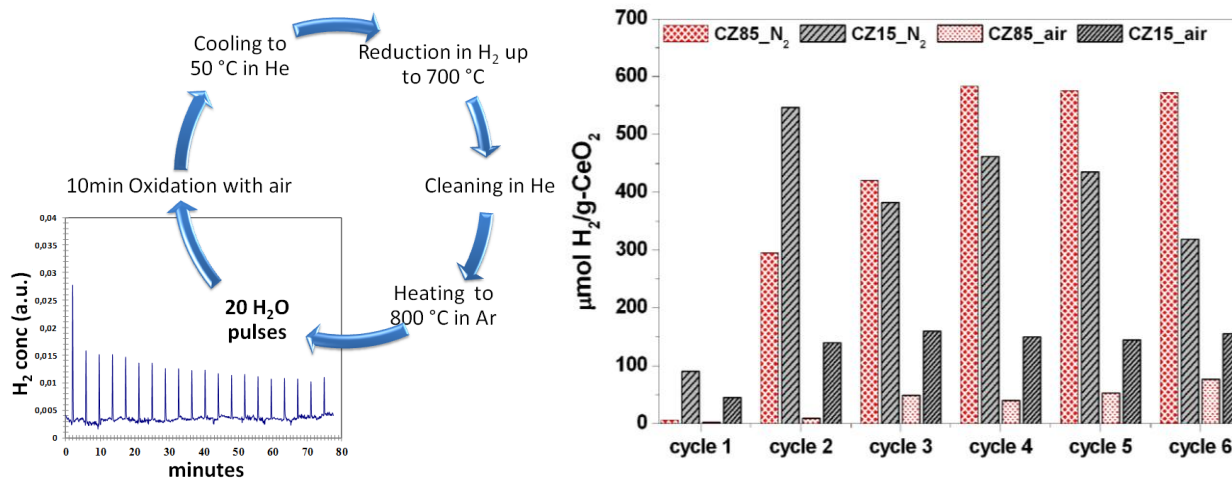


Figure 1: Comparison between water splitting reactivity of CZ85 and of CZ15²⁷ pretreated in N₂ or Air at 1300 °C/4h. On the right, schematic of one typical cycle.

621

622

623

624

625

626

627

628

629

630

631

632

633

634

635

636

637

638

639

640

641

642

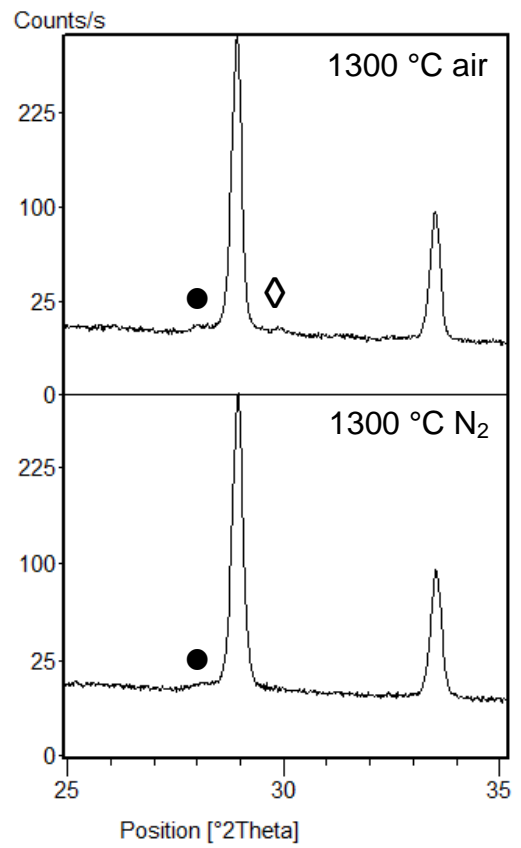
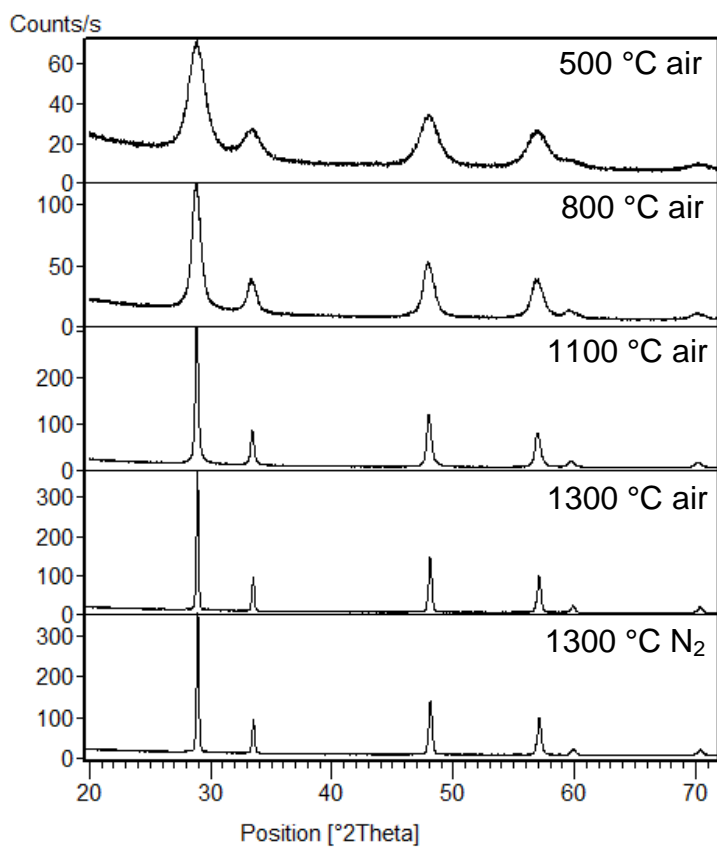
643

644

645

646

647



648 **Figure 2:** X-ray profiles of $\text{Ce}_{0.85}\text{Zr}_{0.15}\text{O}_2$ calcined at different temperatures in air and at 1300 °C in
649 N_2 flow. To the right: details of samples treated at 1300 °C/4h. Symbols indicate the segregated
650 crystal phases : ● $\text{Ce}_{0.05}\text{Zr}_{0.95}\text{O}_2$ (PDF 88-2392); ◇ $\text{Ce}_{0.18}\text{Zr}_{0.82}\text{O}_2$ (PDF 80-0785).

651

652

653

654

655

656

657

658

659

660

661

662

663

664

665

666

667

668

669

670

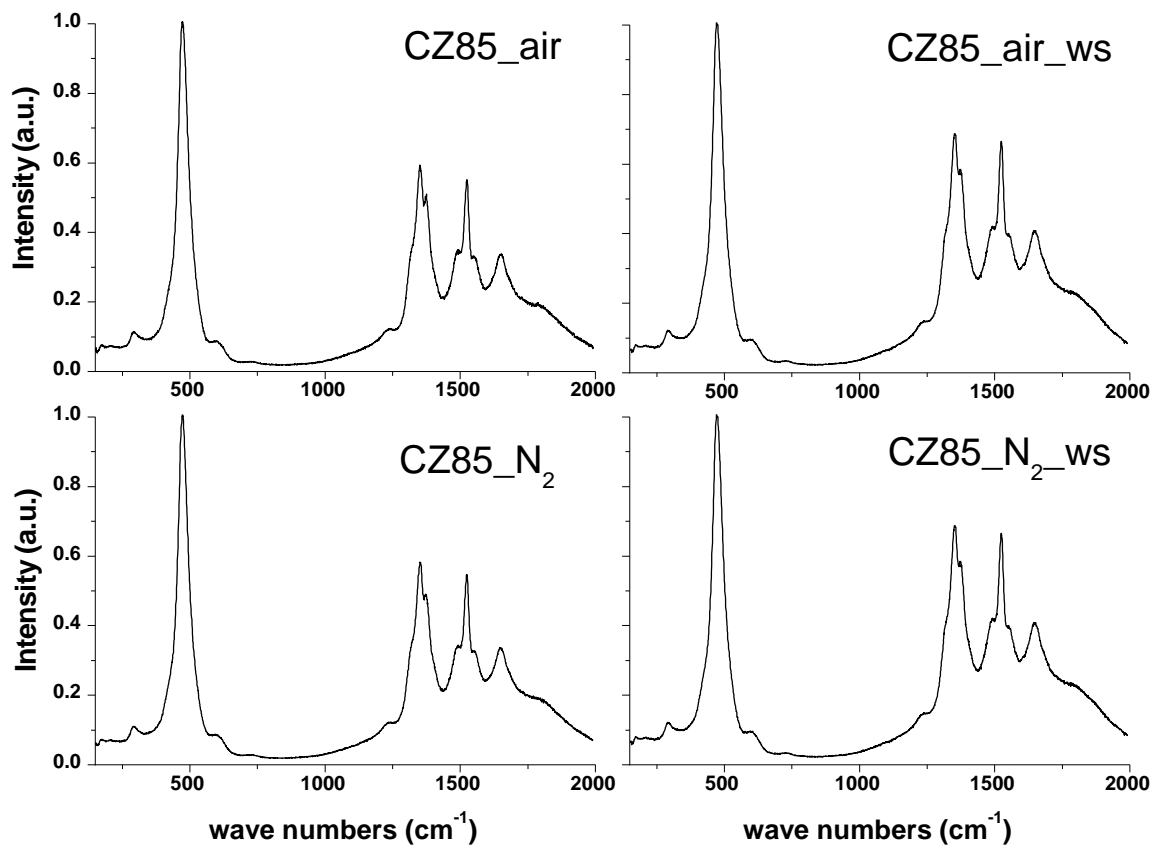
671

672

673

674

675



676

677

678 **Figure 3:** Raman spectra of CZ85 treated in air before(CZ85_air) and after six water splitting
679 cycles (CZ85_air_ws) or in N₂ before (CZ85_N₂) and after six water splitting cycles
680 (CZ85_N₂_ws). Spectra collected using an excitation radiation at 785 nm.

681

682

683

684

685

686

687

688

689

690

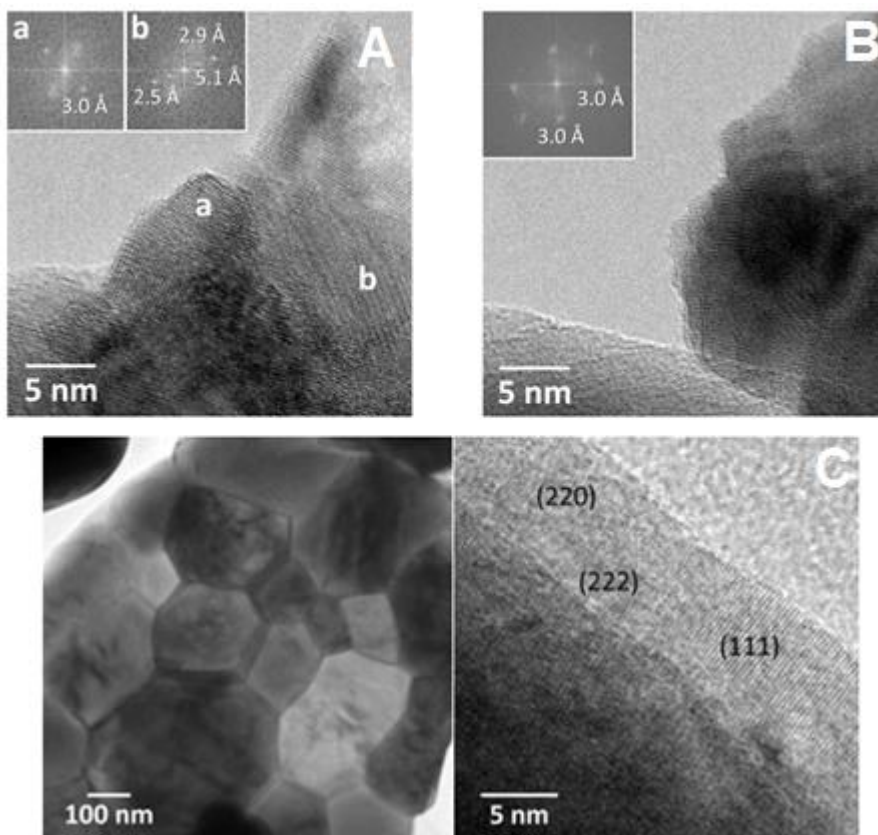
691

692

693

694

695



696

697

698

699

700

701

702

703 **Figure 4:** HRTEM of Ce_{0.85}Zr_{0.15}O₂ (CZ85) treated at 1300 °C/4h: A) in N₂; B) in air; C) images of
704 the sample treated in N₂ after water splitting test.

705

706

707

708

709

710

711

712

713

714

715

716

717

718

719

720

721

722

723

724

725

726

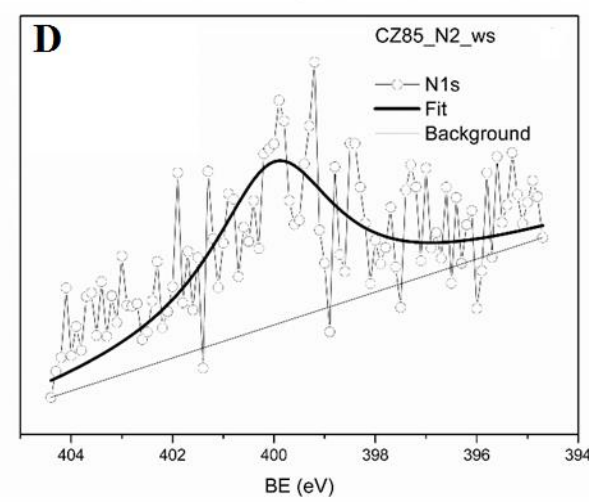
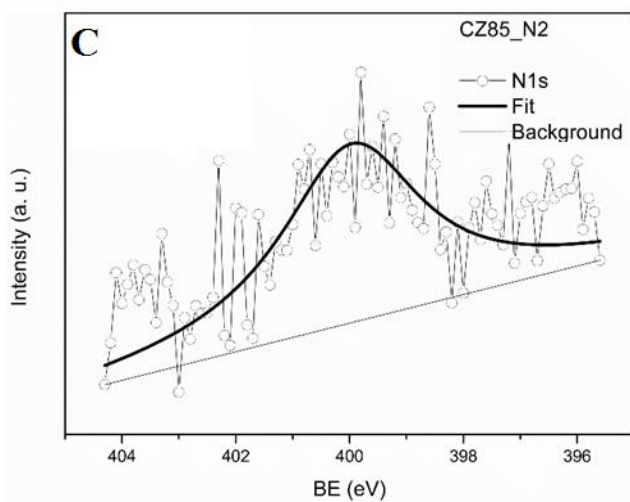
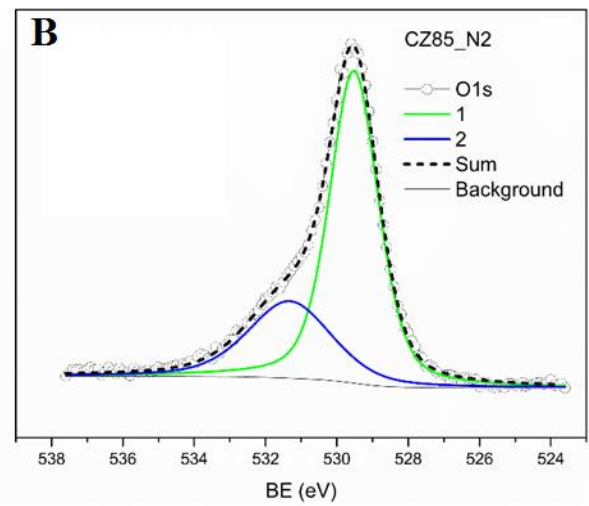
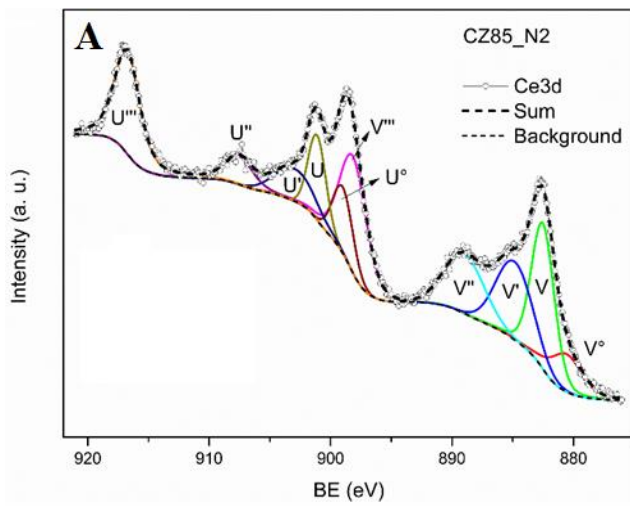
727

728

729

730

731



732

733

734

735

736 **Figure 5:** XPS spectra of CZ85 treated in N₂ 1300 °C/4h. Figures show Ce3d, O1 and N1s regions
737 and related fitting components.

738

739

740

741

742

743

744

745

746

747

748

749

750

751

752

753

754

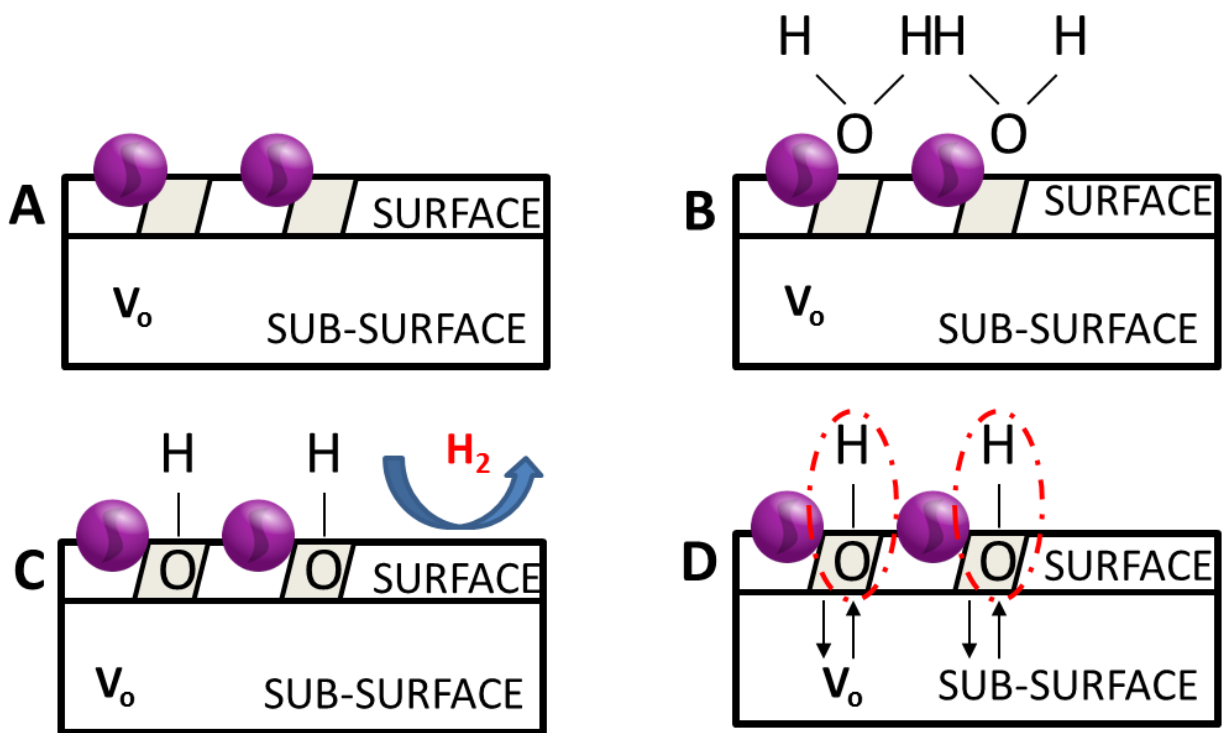
755

756

757

758

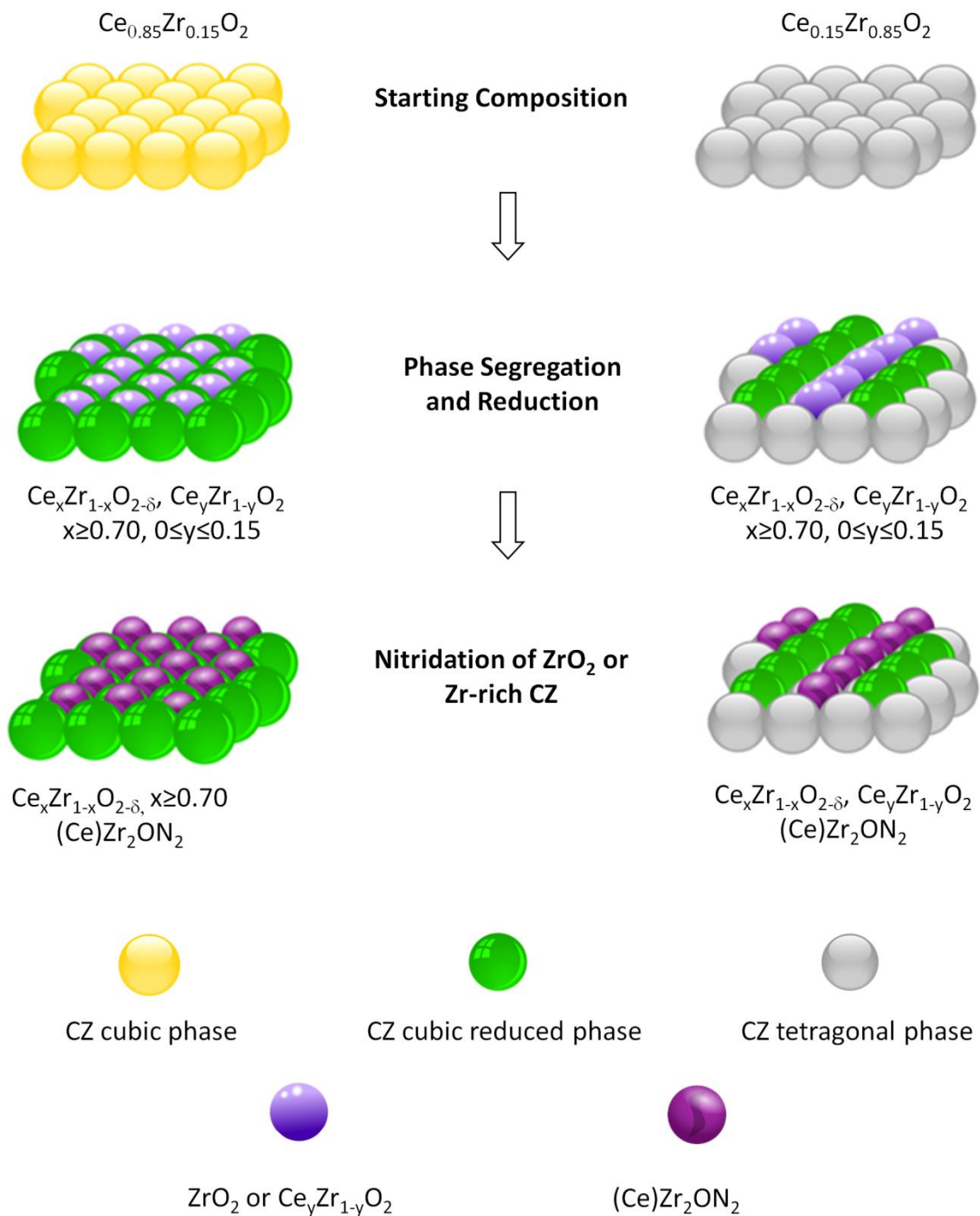
759



Vacancy clusters
 V_o Oxygen vacancies
 (Ce)Zr₂ON₂

760 **Figure 6:** Surface activation mechanism of CZ80 doped with a zirconium oxynitride phase: A)
 761 (Ce)Zr₂ON₂ contributes to form and stabilize large vacancy clusters (VC) on the surface; B-C) water
 762 is adsorbed on VCs forming surface hydroxyl groups (OHs), D) hydroxylated clusters favour the
 763 incorporation of OHs into the subsurface layers and oxygen vacancies migration from the bulk, such
 764 configuration boosts the production of H₂ from the second redox cycle.

765



766

767

768 **Figure 7:** Schematic of segregation processes at 1300 °C in N₂ atmosphere of CZ85 and CZ15.

769

770

771

772 **TABLE OF CONTENTS (TOC) IMAGE**

773

774

775

776

777

